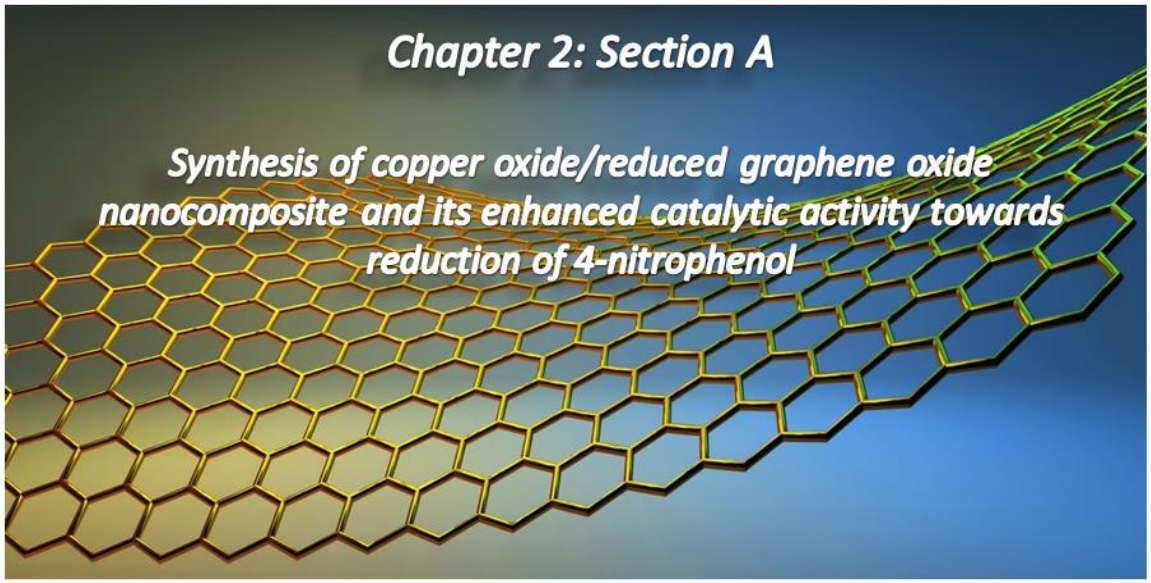

GRAPHICAL ABSTRACT

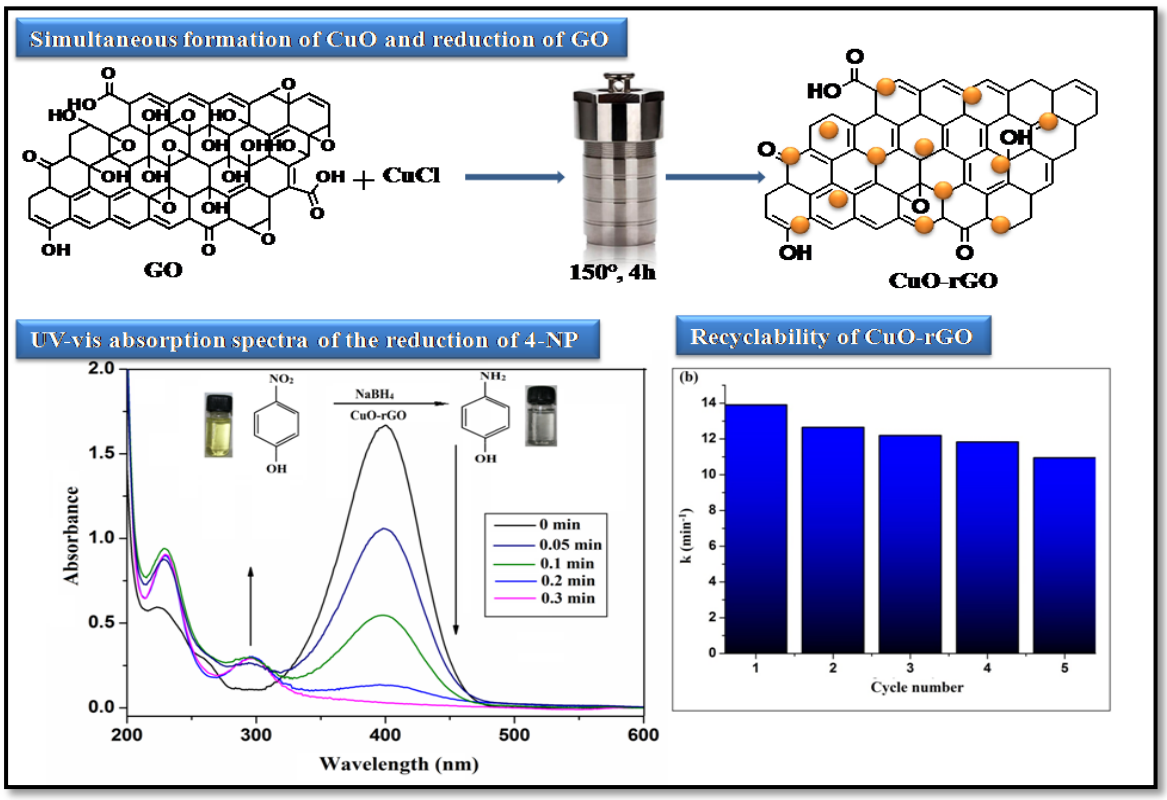

CuO-rGO nanocomposite exhibits excellent and stable catalytic activity towards reduction of 4-nitrophenol to 4-aminophenol with high rate constant value of 13.951 min^{-1}.

2.1 Synthesis of copper oxide/reduced graphene oxide nanocomposite and its enhanced catalytic activity towards reduction of 4-nitrophenol

2.1.1 Introduction

Graphene has attracted tremendous interest in recent years in many fields of science and engineering since it was first reported in 2004 [1, 2]. This interest can be attributed to the extraordinary electrical, optical, thermal, mechanical and chemical properties of graphene and its related carbon nanostructures [3-6]. In addition, it possesses high thermal conductivity, excellent mobility of charge carriers, large specific surface area, good mechanical stability, good biocompatibility and high adsorption capacity [7-11]. To date, various synthetic strategies have been developed for producing graphene such as micromechanical exfoliation, oxidation/reduction protocols, epitaxial growth, and chemical vapour deposition [12, 13.] Graphene and its derivatives have been used over a wide range of applications, including electrocatalysis [14], catalytic oxidation reaction [15], photocatalysis [16], memory devices [17], energy storage [18], solar cells [19], sensing platforms [20], raman enhancement [21] and even in drug delivery [22]. GO does the common choice over pristine graphene owe to its facile synthetic nature in a controlled, scalable, and reproducible manner. Also, its abundant oxygen-containing functional groups such as epoxide, alcohol, and carboxylic acids provide GO with excellent aqueous dispersity and offer anchors for further chemical modifications [23]. In catalysis, graphene-based materials are used as catalytic supports due to their high electrical, thermal conductivity, great mechanical strength, huge specific surface area and good adsorption capacities. GO nanosheets are also emerging as promising supports for the creation of hybrid nanomaterials and, in particular, in catalytic applications.

A variety of metal, metal oxide, semiconducting, and magnetic nanoparticles including Pd [24], Pt [25], Au [26], TiO_2 [27] and Fe_3O_4 [28] have been hosted on the surface of GO. Nanoparticles can act as spacers between GO nanosheets to minimize the agglomeration of them and can also prevent the aggregation of these active nanoblocks with high surface energy. The nanocomposites often exhibit enhanced properties and

---

This part of the thesis is published in

Sarkar, C. and Dolui, S. K. RSC Advances, 5(75):60763-60769, 2015.

improved functionalities due to the synergetic effects between GO nanosheets and the nanoparticles [29, 30]. Most of these hybrid nanocomposites find applications as electrocatalysts. However, a few papers have reported on their catalytic activity for organic transformation [24]. For example, Choi and co-workers have reported the catalytic activity of Au nanoparticles supported on GO for catalytic reduction of nitroarenes [31]. Compared with the expensive noble metal or metal oxide nanoparticles CuO is a cheap alternative with broad potential applications. It has been widely used in active anode materials, superconductors, sensors and heterogeneous catalysts due to its abundant resources, environmental compatibility, cost effectiveness and favorable pseudocapacitive characteristics [32, 33]. Integrating nanoparticles into graphene currently has been an active research field. Zhao et al. [34] has synthesized CuO-graphene nanostructure by a hydrothermal method in presence of ammonia solution for use in supercapacitors. CuO-graphene nanocomposites are also exhibited high capacity and capacity retention as anode materials in lithium ion batteries [34, 35]. To the best of our knowledge, there is no research studying their catalytic application.

Herein, we present a simple and facile approach for integrating CuO onto the surface of rGO by hydrothermal method. During the hydrothermal treatment, GO was successfully reduced to rGO and CuCl was oxidized to CuO due to the redox reaction. This method eliminates the use of toxic reducing agents and offers the necessary stability of the resulting nanocomposite for catalytic transformation. Furthermore, the resulting CuO-rGO nanocomposites exhibit excellent catalytic activity toward the reduction of 4-NP in presence of $NaBH_4$. The catalytic activities of the nanocomposites were also studied by changing the ratio of GO and Cu. The reaction was completed in only 20 s at room temperature and the catalyst can be easily regenerated and reused with good recyclability up to five catalytic cycles. Considering the wide-ranging potential applications of rGO as a host material for a variety of nanoparticles, the approach developed here may lead to new possibilities for the fabrication of rGO by nanomaterials endowed with multiple functionalities.

2.1.2 Experimental Section

2.1.2.1 Chemicals

Graphite power (<20 micron, Aldrich) was used as received. Sodium nitrate ($NaNO_3$), potassium permanganate ($KMnO_4$), hydrogen peroxide (50% v/v), cuprous

chloride (CuCl), 4-nitrophenol, sodium borohydride ($NaBH_4$), concentrated sulfuric acid (98%), hydrochloric acid were procured from Merck.

2.1.2.2 Preparation of GO and CuO-rGO nanocomposites

GO was synthesized from natural graphite powder using modified Hummers method [36]. CuO-rGO nanocomposites was synthesized by hydrothermal method from mixture of GO and CuCl. In this process, 10.0 mg of GO was dispersed in 10.0 mL of distilled water and 9.89mg of CuCl (0.01 mol CuCl in 1000 mg GO, labelled as $CuO_{0.01}$-rGO) was dispersed with 20mL distilled water by ultrasonication to form a homogeneous dispersion. Then, the GO dispersion was gradually added to the CuCl solution. The solution mixture was stirred magnetically at 25 °C for 120 min and transferred into an autoclave with a volume of 50 mL. Hydrothermal treatment of the mixed solution was done at 150 °C for 4 h, and the solid product was washed with distilled water by centrifugation several times. Then, the composites were dried at 100 °C to obtain the desired CuO-rGO nanocomposites. In addition, for optimization, 0.05 mol CuCl in 1000 mg ($CuO_{0.05}$-rGO) and 0.1 mol CuCl in 1000 mg ($CuO_{0.1}$-rGO) was also synthesized following the same procedure.

2.1.2.3 Characterization

The infrared spectra were recorded with samples on KBr pellets over a frequency range of 4000-500 cm^{-1} in a Nicolet model impact 410 FT-IR Spectrophotometer. The X-ray diffraction (XRD) study was carried out at room temperature (ca. 298 K) using a Rigaku X-ray diffractometer with Cu-*K*α radiation (λ= 0.15418nm) at 30 kV and 15 mA using a scanning rate of 0.05 θ**/sec** in the range of 2θ = (10°-70°). The morphology of CuO-rGO nanocomposites was characterized with scanning electron microscope (SEM). The SEM analysis was conducted on JSM-6390LV (Jeol, Japan) Scanning Electron Micrograph attached with energy dispersive X-ray detector. Scanning was done at micrometer range; images were taken at an accelerating voltage of 15-20kV with magnification of ×15,000 and ×20,000 and data were obtained by using INCA software.

2.1.2.4 Catalytic Reduction of p-nitrophenol (4-NP) by CuO-rGO nanocomposite

In a typical reaction, freshly prepared aqueous solution of $NaBH_4$ (0.1 mL, 0.3 M) was added in 10.0 mL of 4-NP aqueous solution (1×10^{-4} M). This was leading to a

color change from light yellow to yellow green. To that solution, 1.0 mg catalyst was added and the reaction solution was allowed to stir until the solution became colorless. The green yellow color of the solution gradually vanished, indicating the reduction of 4-NP. The reaction progress was checked by assessing a small portion of the reaction mixture at a given time interval. The concentration of 4-NP was recorded in the UV−vis spectrophotometer at a wavelength of 400 nm.

To study the recycling ability of the catalyst, the catalyst was separated from the solution by centrifugation and washed with distilled water several times. Then the catalyst was added into another freshly prepared mixed solution of 4-NP and $NaBH_4$ to start the next round of reaction. The recyclability test was carried out for five catalytic cycles.

2.1.3 Results and discussion

2.1.3.1 Characterization of CuO-rGO nanocomposite

2.1.3.1.1 FTIR study

Fig.2.1.1 shows the FTIR spectra of GO, CuCl and CuO-rGO nanocomposite. In the FTIR spectrum of GO (Fig.2.1.1a), the peaks obtained at 1264 cm^{-1}, 1067 cm^{-1} and 1721 cm^{-1} are attributed to the C–O epoxy stretching, C-O alkoxy stretching and C=O carbonyl stretching vibrations, respectively. The absorption band at 1623 cm^{-1} and 3421 cm^{-1} corresponds to the aromatic C=C stretching vibration and O-H stretching vibration respectively. Normally, CuCl vibrations are observed at wavenumbers less than 500 cm^{-1}[37]. In the FTIR spectrum of CuCl (Fig.2.1.1b), peak at 442 cm^{-1} corresponds to Cu-Cl stretching vibration. Bands at 3408 cm^{-1} and 3342 cm^{-1} may be attributed to the Cu-OH groups. Peaks between 500 cm^{-1} to 1500 cm^{-1} is made for the observation of hydroxyl deformation modes. In the FTIR spectrum of CuO-rGO nanocomposite (Fig.2.1.1c), the peak intensity of C=O, C-OH, and C-O groups decreases significantly, indicating reduction of GO. Again, some new peaks appeared at 576 cm^{-1}, 505 cm^{-1} and 453 cm^{-1} corresponding to Cu-O stretching vibrations. These results implied simultaneous reduction of GO along with formation of CuO by hydrothermal treatment.

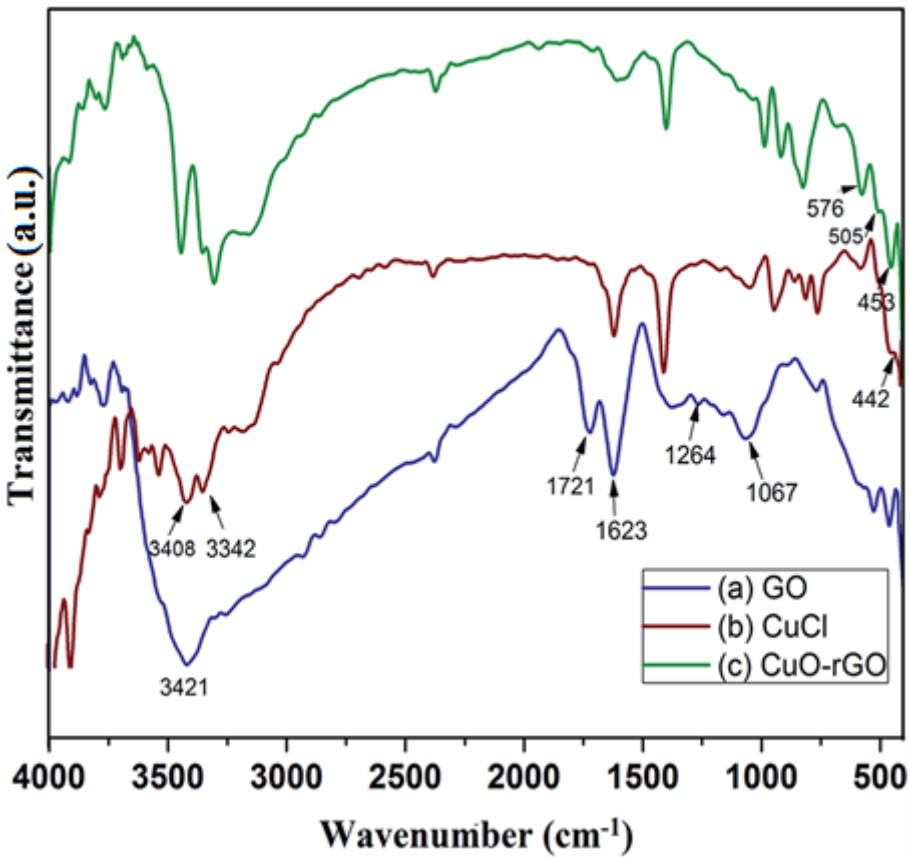

Fig.2.1.1 FTIR spectrum of (a) GO, (b) CuCl and (c) CuO-rGO nanocomposite

2.1.3.1.2 XRD analysis

Fig.2.1.2 shows XRD patterns of GO, CuCl and CuO-rGO nanocomposite. GO exhibited the strong diffraction peak at $2\theta = 11.45^{o}$ (Fig.2.1.2a), attributed to the (001) plane due to oxygen containing functional groups on carbon sheets. In the XRD pattern of CuCl and CuO-rGO, the positions of diffraction peaks matched well with standard CuCl, CuO and rGO. The peaks at 2θ values of 28.45° (111), 47.35° (220), 56.2° (311) and 68.5° (400) were consistent with the standard XRD data for the CuCl cubic phase of face centered crystal lattice (JCPDS Card no. 82-2114, Fig.2.1.2b). The XRD spectra of CuC-GO exhibits peaks at 2θ values of 32.55° (110), 39.95° (111), 50.25° (112), 53.85° (020), 58.5° (202) and 63.6° (113) which were consistent with the standard XRD data for the CuO monoclinic phase of end-centered crystal lattice (JCPDS Card no. 89-2530, Fig.2.1.2c). Again, the spectrum shows small additional peaks at 25.2° and 44.9° which could be attributed to rGO. These results demonstrated that GO was successfully reduced to rGO and CuCl was oxidized to CuO during the redox reaction.

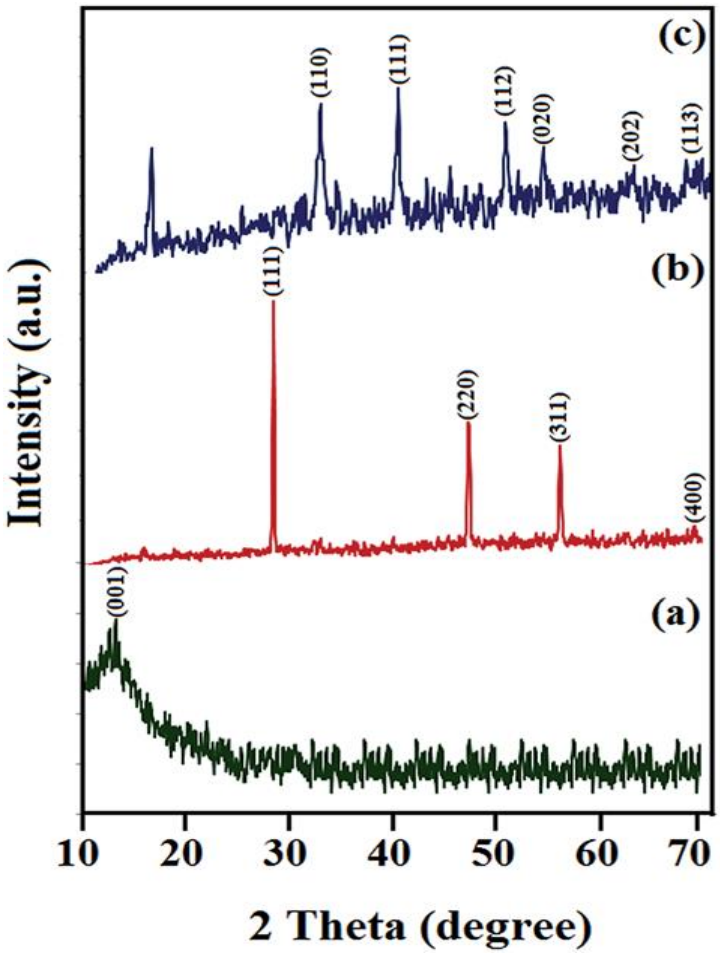

Fig.2.1.2 XRD patterns of (a) GO, (b) CuCl and (c) CuO-rGO nanocomposite

2.1.3.1.3 SEM and EDX analysis

A difference in surface morphology between CuCl and CuO-rGO nanocomposite is observed (Fig.2.1.3). The SEM image of CuO-rGO revealed that the copper nanoparticles are homogeneously distributed over crumpled, paper-like surface of GO confirming that the incorporation of Cu nanoparticle into GO (Fig.2.1.3b). Again, the EDX spectrum of CuO-rGO (Fig.2.1.4) exhibited the presence of C, O, and Cu elements, further confirming the formation of CuO-rGO nanocomposite.

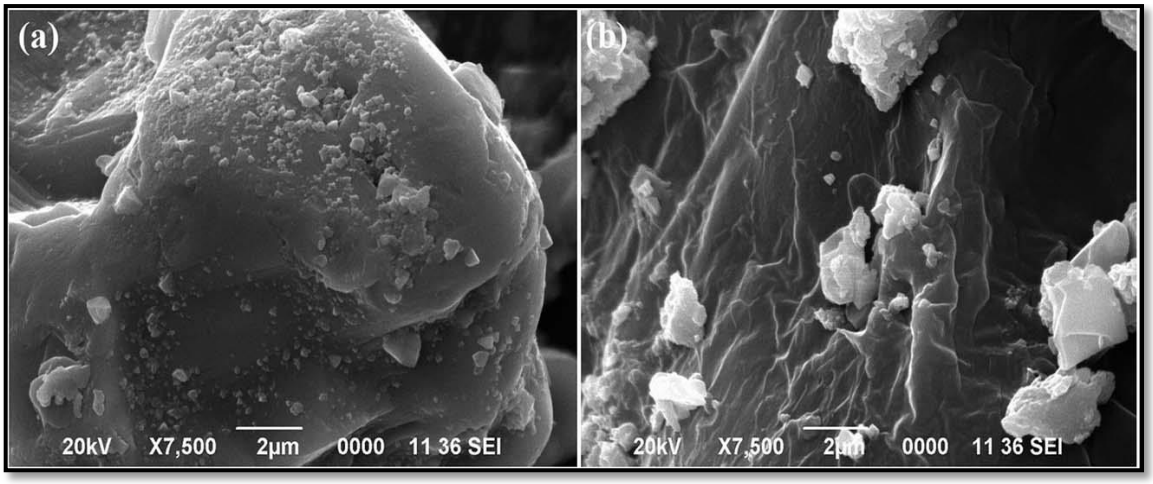

Fig.2.1.3 SEM images of (a) CuCl and (b) CuO-rGO nanocomposite

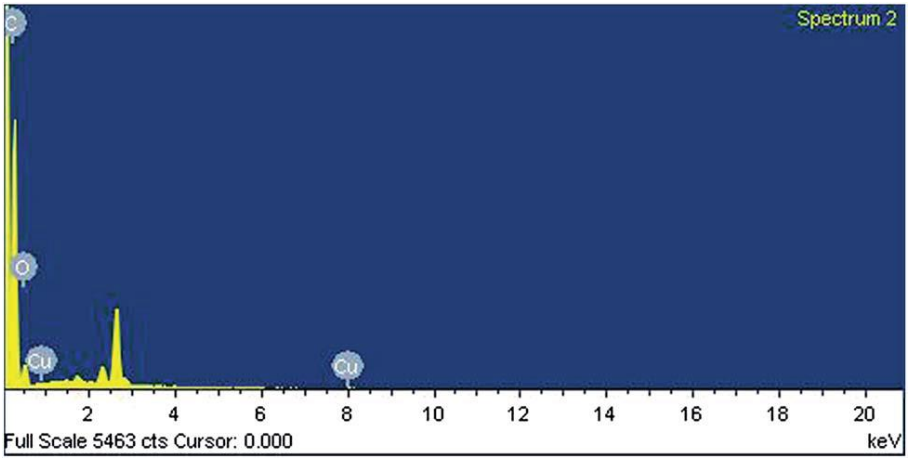

Fig.2.1.4 EDX spectrum of CuO-rGO nanocomposite

2.1.3.2 Catalytic properties of CuO-rGO nanocomposite

The catalytic properties of the CuO-rGO nanocomposite were quantitatively evaluated with the reduction 4-NP into of 4-aminophenol (4-AP) by $NaBH_4$ as a model system. As shown in fig.5, this reaction could be easily monitored by the time-dependent UV−vis absorption spectra. In the absence of the catalysts, the mixture of 4-NP and $NaBH_4$ show a strong peak at 400 nm due to the formation of 4-NP ions under alkaline condition. After the catalysts were added into the system, the absorption peak of 4-NP at 400 nm decreases rapidly with a concomitant increase in the peak at 300 nm, which is attributed to the reduced product, 4-AP. As the initial concentration of $NaBH_4$ is large excess in comparison to 4-NP, the pseudo-first-order reaction kinetics was applied for the evaluation of the catalytic rate. Therefore, the kinetic equation can be written as:

$$\ln(C/C_0) = -kt$$

where C_0 is the initial concentration of 4-NP in absence of catalyst; C is the concentration of 4-NP at any time, t after catalyst was added; and '*k*' is the rate constant, which can be obtained from the decrease in the peak intensity at 400 nm with time.

Fig.2.1.5 shows the UV-vis absorption spectra of the reduction of 4-NP by $NaBH_4$ and fig.6 shows the corresponding plots of $\ln(C/C_0)$ of 4-NP *versus* reaction time in the presence of (a) $CuO_{0.01}$ -rGO (b) $CuO_{0.05}$ -rGO (c) $CuO_{0.1}$ –rGO. From the linear relations of $\ln(C/C_0)$, shown in Fig.2.1.6, the maximum value of rate constant, *k*, for this reaction is 13.951 min^{-1}, which is very high compared to those reported previously (Table 2.1.2). The results are summarized in table 2.1.1 Good linear correlations (R^2 > 0.996) of $\ln(C/C_0)$ *vs. t* are observed for all nanocomposites, confirming the pseudo-first-order kinetics (Table 2.1.1)

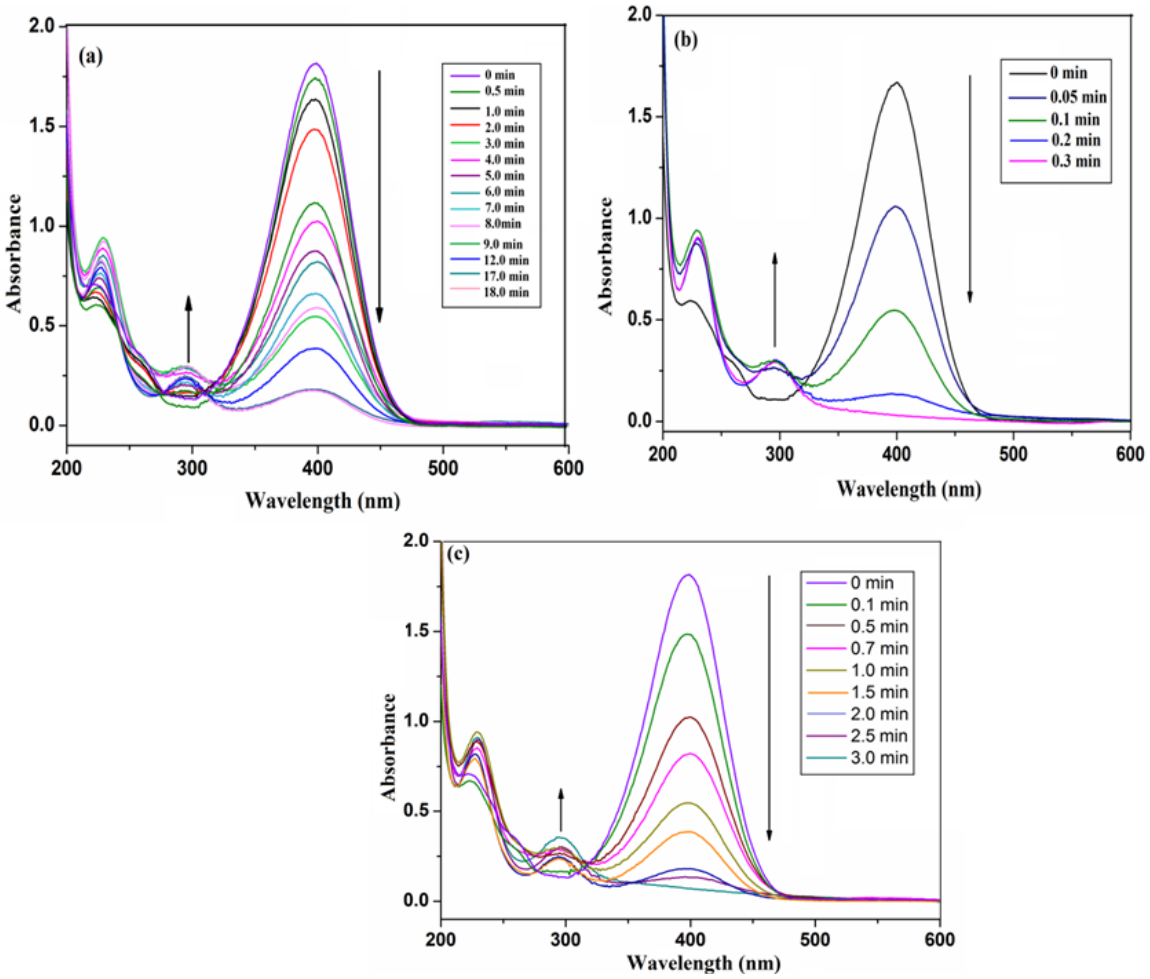

Fig.2.1.5 UV-vis absorption spectra of the reduction of 4-NP by $NaBH_4$ in the presence of (a) $CuO_{0.01}$ -rGO (b) $CuO_{0.05}$ -rGO (c) $CuO_{0.1}$-rGO.

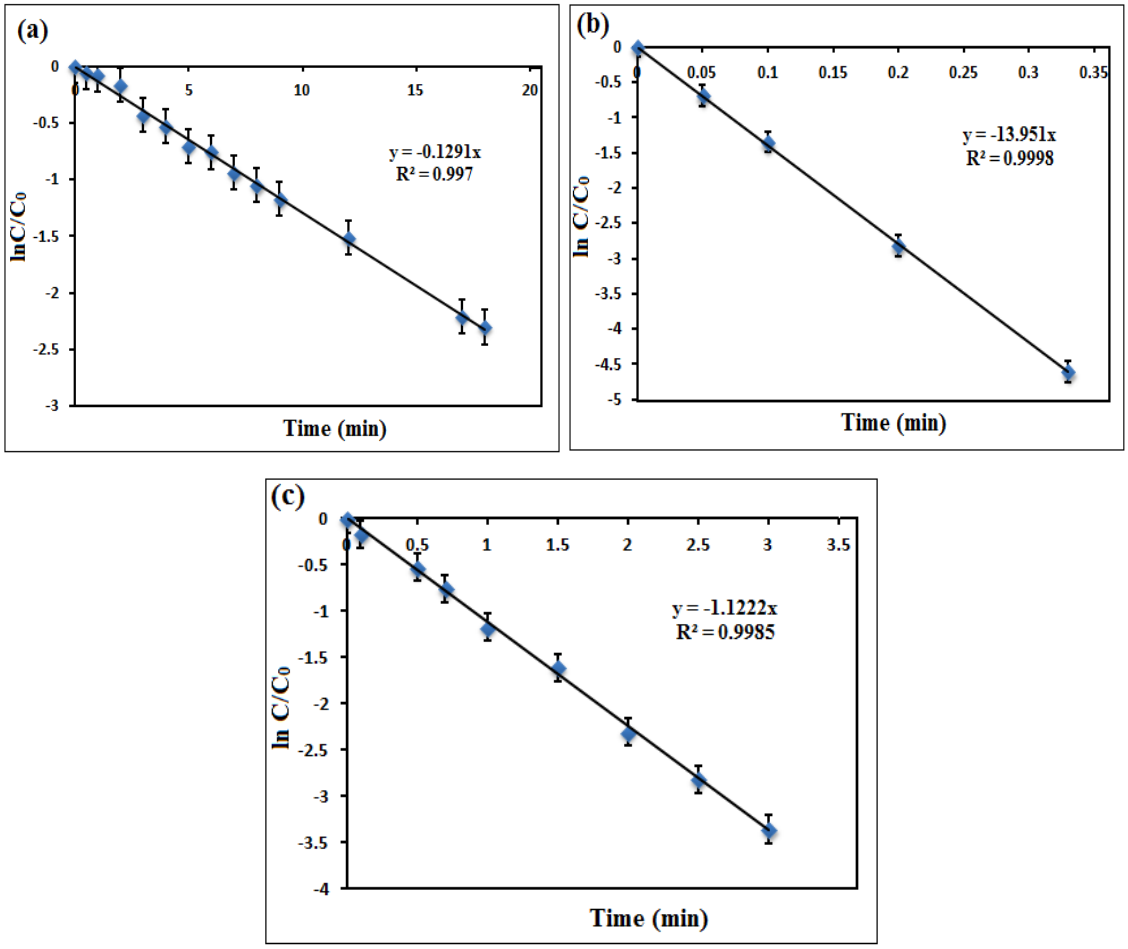

Fig.2.1.6 Plots of ln(C/C_0) of 4-NP versus reaction time in the presence of (a) $CuO_{0.01}$ -rGO (b) $CuO_{0.05}$ -rGO (c) $CuO_{0.1}$–rGO.

Table 2.1.1 Catalytic rate constants of reduction of 4-NP in the presence of CuO_x-rGO nanocomposites and the R^2 values for the ln(C/C_0) vs t plots

Entry	Catalyst	4-NP (M)	$NaBH_4$ (M)	Rate Constant (min^{-1})	R^2
1	$CuO_{0.01}$ –rGO	1×10^{-4}	0.3	0.1237	0.9259
2	$CuO_{0.05}$ –rGO	1×10^{-4}	0.3	13.9	0.9999
3	$CuO_{0.1}$ –rGO	1×10^{-4}	0.3	1.12	0.9996

It should be noted that the $CuO_{0.05}$–rGO shows the highest catalytic activity with only 20 s to finish the reaction (Fig.2.1.5b), whereas $CuO_{0.01}$–rGO shows the lowest catalytic activity and can't achieve the full reduction of 4-NP even with a reaction time of 18 min (Fig.2.1.5a). On the other hand, $CuO_{0.1}$–rGO required 3 min to finish the reaction. The higher catalytic activity for the CuO–rGO catalysts is may be ascribed to

the two dimensional structure of rGO, which has a high affinity for the adsorption of 4-NP due to π–π stacking interactions. This increases the concentration of 4-NP near CuO. The high catalytic activity occurs from the synergistic effect of: (1) the high adsorption ability of rGO towards 4-NP, providing a high concentration of 4-NP near to the CuO which accelerates the reaction; and (2) electron transfer from rGO to CuO, facilitating the uptake of electrons by 4-NP molecules. Thus, the catalytic activity of the CuO–rGO catalyst depends on both CuO and rGO. With increase in the amount of CuO the catalytic activity increase and after a certain amount the activity decreases. This may be due to the decrease in the available active surface of rGO for adsorption of 4-NP.

The representative sample of $CuO_{0.05}$-rGOwas also tested for reusability in the reduction of 4-NP by $NaBH_4$. The catalyst was separated by centrifugation and reused to carry out the reduction process for an additional four times. After the completion of five cycles, the values of *k* for each round of catalytic reaction were obtained from the plots of $\ln(C/C_0)$ vs t (Fig.2.1.7a). The *k* values for the successive five cycles was shown in Fig.2.1.7b, there is only a slight decrease in the *k* value with the increasing cycle. The main reason for the decrease in the catalytic activity is loss of catalyst during the separation process.

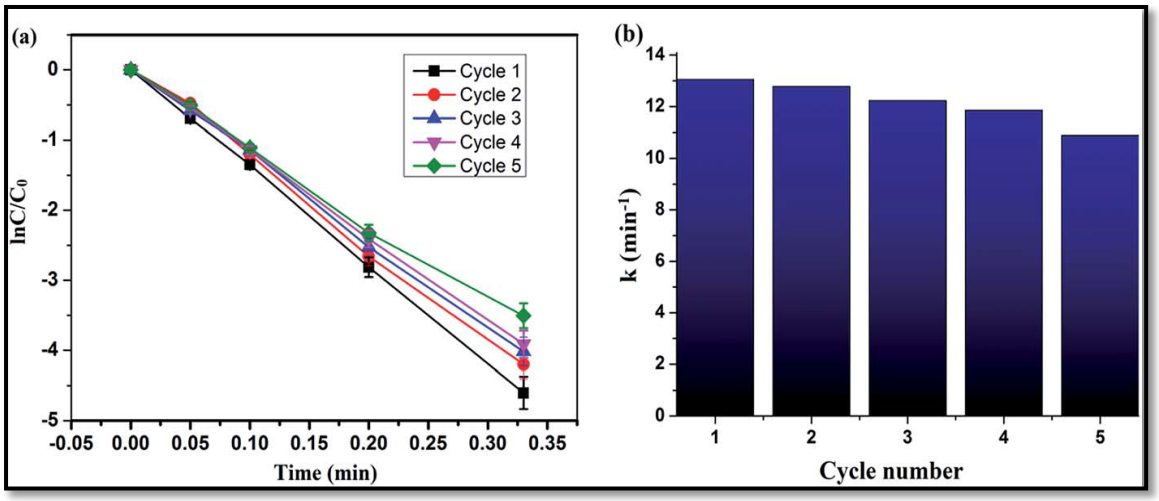

Fig.2.1.7 (a) Plots of ln(C/Co) of 4-NP versus reaction time for successive 5 cycles (b) Value of *k* for each cycle with CuO-$rGO_{0.05}$ nanocomposite as catalyst.

2.1.4 Comparison with other catalysts

For the comparison of the present work with some of the earlier reports, different catalysts employed for the catalytic reduction of 4-NP are highlighted in Table 2.1.2. It is

evident from Table 2.1.2 that the value of *k* of present work is much larger than Cu nanocatalyst [38] and pristine GO [37]. The catalytic activity of the synthesized catalyst is superior compared to all other metal nanocatalysts as well as noble metal/GR based catalysts reported earlier [38, 31].

Table 2.1.2 Comparison of values of rate constant for 4-NP reduction to 4-AP catalyzed by various catalysts.

Entry	Catalyst	4-NP (M)	$NaBH_4$ (M)	*k* (min^{-1})	Ref.
1	$CuO_{0.05}$-rGO	1×10^{-4}	0.3	13.9	Present work
2	Cu nanoparticle	1.2×10^{-4}	0.02	0.095	38
3	Au nanocages Au nanoboxes Au nanoparticles	1.4×10^{-4} 1.4×10^{-4} 1.4×10^{-4}	0.042 0.042 0.042	5.58 (at 43° C) 3.25 (at 43° C) 0.95	39
4	Au-GR hydrogel	1×10^{-3}	0.1	0.19	40
5	Au-rGO Au GO	7.5×10^{-4}	2.22	6.478 0.069 0.038	31
6	Au-Ag/GO Au/GO Ag/GO	1.54×10^{-3}	0.88	8.56 0.368 0.208	41

2.1.5 Conclusion

In summary, a facile and novel method to prepare rGO-supported CuO nanoparticles was successfully developed. The prepared nanocomposite is successfully employed in the catalytic reduction of 4-NP with excellent catalytic activities and stabilities by the synergistic catalytic effect of CuO nanoparticle and rGO, further highlighting the importance of hybrid CuO-rGO nanocomposites. Considering the wide applications of rGO as a host material for a variety of nanoparticles, the present approach

may lead to new possibilities for integrating active nanoparticles with rGO for advanced electronic, energy, and catalytic applications.

2.1.6 References

[1] Novoselov, K. S., Geim, A. K., Morozov, S. V., Jiang, D., Zhang, Y., Dubonos, S. V., Grigorieva, I. V., and Firsov, A. A. Electric field effect in atomically thin carbon films. *Science*, 306(5696):666-669, 2004.

[2] Rao, C. N. R., Sood, A. K., Subrahmanyam, K. S., and Govindaraj, A. Graphene: the new two-dimensional nanomaterial. *Angewandte Chemie International Edition*, 48(42):7752-7777, 2009.

[3] Stankovich, S., Dikin, D. A., Dommett, G. H., Kohlhaas, K. M., Zimney, E. J., Stach, E. A., Piner, R. D., Nguyen, S. T., and Ruoff, R. S. Graphene-based composite materials. *Nature*, 442(7100):282-286, 2006.

[4] Balandin, A. A., Ghosh, S., Bao, W., Calizo, I., Teweldebrhan, D., Miao, F., and Lau, C. N. Superior thermal conductivity of single-layer graphene. *Nano letters*, 8(3):902-907, 2008.

[5] Lee, Z., Jeon, K. J., Dato, A., Erni, R., Richardson, T. J., Frenklach, M., and Radmilovic, V. Direct imaging of soft-hard interfaces enabled by graphene. *Nano letters*, 9(9):3365-3369, 2009.

[6] Loh, K. P., Bao, Q., Eda, G., and Chhowalla, M. Graphene oxide as a chemically tunable platform for optical applications. *Nature chemistry*, 2(12):1015-1024, 2010.

[7] Balandin, A. A. Thermal properties of graphene and nanostructured carbon materials. *Nature materials*, 10(8):569-581, 2011.

[8] Novoselov, K. S. and Geim, A. K. The rise of graphene. *Nature Mater*, 6(3):183-191, 2007.

[9] Allen, M. J., Tung, V. C., and Kaner, R. B. Honeycomb carbon: a review of graphene. *Chemical reviews*, 110(1):132-145, 2009.

[10] Duch, M. C., Budinger, G. S., Liang, Y. T., Soberanes, S., Urich, D., Chiarella, S. E., Campochiaro, L. A., Gonzalez, A., Chandel, N. S., Hersam, M. C., and Mutlu, G. M. Minimizing oxidation and stable nanoscale dispersion improves the biocompatibility of graphene in the lung. *Nano letters*, 11(12):5201-5207, 2011.

[11] Xu, J., Wang, L., and Zhu, Y. Decontamination of bisphenol A from aqueous solution by graphene adsorption. *Langmuir*, 28(22):8418-8425, 2012.

[12] Eda, G., Fanchini, G., and Chhowalla, M. Large-area ultrathin films of reduced graphene oxide as a transparent and flexible electronic material. *Nature nanotechnology*, 3(5):270-274, 2008.

[13] Kim, K. S., Zhao, Y., Jang, H., Lee, S. Y., Kim, J. M., Kim, K. S., Ahn, J. H., Kim, P., Choi, J. Y., and Hong, B. H. Large-scale pattern growth of graphene films for stretchable transparent electrodes. *Nature*, 457(7230):706-710, 2009.

[14] Yu, F., Ma, J. and Bi, D. Enhanced adsorptive removal of selected pharmaceutical antibiotics from aqueous solution by activated graphene. *Environmental Science and Pollution Research*, 22(6):4715-4724, 2015.

[15] Kong, X. K., Chen, C. L., and Chen, Q. W. Doped graphene for metal-free catalysis. *Chemical Society Reviews*, 43(8):2841-2857, 2014.

[16] Zhang, N., Zhang, Y., and Xu, Y.J. Recent progress on graphene-based photocatalysts: current status and future perspectives. *Nanoscale*, 4(19):5792-5813, 2012.

[17] Gunlycke, D., Areshkin, D. A., Li, J., Mintmire, J. W., and White, C. T. Graphene nanostrip digital memory device. *Nano letters*, 7(12):3608-3611, 2007.

[18] Mishra, A. K. and Ramaprabhu, S. Functionalized graphene-based nanocomposites for supercapacitor application. *The Journal of Physical Chemistry C*, 115(29):14006-14013, 2011.

[19] Roy-Mayhew, J. D. and Aksay, I.A. Graphene materials and their use in dye-sensitized solar cells. *Chemical reviews*, 114(12):6323-6348, 2014.

[20] Schedin, F., Geim, A. K., Morozov, S. V., Hill, E. W., Blake, P., Katsnelson, M. I., and Novoselov, K. S. Detection of individual gas molecules adsorbed on graphene. *Nature materials*, 6(9):652-655, 2007.

[21] Ling, X., Xie, L., Fang, Y., Xu, H., Zhang, H., Kong, J., Dresselhaus, M.S., Zhang, J., and Liu, Z. Can graphene be used as a substrate for Raman enhancement?. *Nano letters*, 10(2):553-561, 2009.

[22] Akhavan, O., Ghaderi, E., and Esfandiar, A. Wrapping bacteria by graphene nanosheets for isolation from environment, reactivation by sonication, and inactivation by near-infrared irradiation. *The Journal of Physical Chemistry B*, 115(19):6279-6288, 2011.

[23] Wei, D. and Liu, Y. Controllable synthesis of graphene and its applications. *Advanced Materials*, 22(30):3225-3241, 2010.

[24] Scheuermann, G. M., Rumi, L., Steurer, P., Bannwarth, W., and Mülhaupt, R. Palladium nanoparticles on graphite oxide and its functionalized graphene derivatives as highly active catalysts for the Suzuki-Miyaura coupling reaction. *Journal of the American Chemical Society*, 131(23):8262-8270, 2009.

[25] Guo, S., Wen, D., Zhai, Y., Dong, S., and Wang, E. Platinum nanoparticle ensemble-on-graphene hybrid nanosheet: one-pot, rapid synthesis, and used as new electrode material for electrochemical sensing. *ACS nano*, 4(7):3959-3968, 2010.

[26] Muszynski, R., Seger, B., and Kamat, P. V. Decorating graphene sheets with gold nanoparticles. *The Journal of Physical Chemistry C*, 112(14):5263-5266, 2008.

[27] Manga, K. K., Wang, S., Jaiswal, M., Bao, Q., and Loh, K. P. High-Gain Graphene-Titanium Oxide Photoconductor Made from Inkjet Printable Ionic Solution. *Advanced Materials*, 22(46):5265-5270, 2010.

[28] Li, B., Cao, H., Shao, J., Qu, M., and Warner, J. H. Superparamagnetic Fe_3O_4 nanocrystals@ graphene composites for energy storage devices. *Journal of Materials Chemistry*, 21(13):5069-5075, 2011.

[29] Li, B., Cao, H., and Yin, G. $Mg(OH)_2$@ reduced graphene oxide composite for removal of dyes from water. *Journal of Materials Chemistry*, 21(36):13765-13768, 2011.

[30] Li, B. and Cao, H. ZnO@ graphene composite with enhanced performance for the removal of dye from water. *Journal of Materials Chemistry*, *21*(10):3346-3349, 2011.

[31] Choi, Y., Bae, H. S., Seo, E., Jang, S., Park, K. H., and Kim, B. S. Hybrid gold nanoparticle-reduced graphene oxide nanosheets as active catalysts for highly efficient reduction of nitroarenes. *Journal of Materials Chemistry*, 21(39):15431-15436, 2011.

[32] Shaikh, J. S., Pawar, R. C., Moholkar, A. V., Kim, J. H., and Patil, P. S. CuO-PAA hybrid films: chemical synthesis and supercapacitor behavior. *Applied Surface Science*, 257(9):4389-4397, 2011.

[33] Zhang, H. and Zhang, M. Synthesis of CuO nanocrystalline and their application as electrode materials for capacitors. *Materials Chemistry and Physics*, 108(2-3):184-187, 2008.

[34] Zhao, B., Liu, P., Zhuang, H., Jiao, Z., Fang, T., Xu, W., Lu, B., and Jiang, Y. Hierarchical self-assembly of microscale leaf-like CuO on graphene sheets for high-performance electrochemical capacitors. *Journal of Materials Chemistry A*, 1(2):367-373, 2013.

[35] Wang, B., Wu, X. L., Shu, C. Y., Guo, Y. G., and Wang, C. R. Synthesis of CuO/graphene nanocomposite as a high-performance anode material for lithium-ion batteries. *Journal of Materials Chemistry*, 20(47):10661-10664, 2010.

[36] Hummers Jr, W. S., and Offeman, R.E. Preparation of graphitic oxide. *Journal of the American Chemical Society*, 80(6):1339-1339, 1958.

[37] Frost, R. L., Martens, W., Kloprogge, J. T., and Williams, P. A. Raman spectroscopy of the basic copper chloride minerals atacamite and paratacamite: implications for the study of copper, brass and bronze objects of archaeological significance. *Journal of Raman Spectroscopy*, 33(10):801-806, 2002.

[38] Deka, P., Deka, R. C., and Bharali, P. In situ generated copper nanoparticle catalyzed reduction of 4-nitrophenol. *New Journal of Chemistry*, 38(4):1789-1793, 2014.

[39] Zeng, J., Zhang, Q., Chen, J., and Xia, Y. A comparison study of the catalytic properties of Au-based nanocages, nanoboxes, and nanoparticles. *Nano letters*, 10(1):30-35, 2009.

[40] Li, J., Liu, C. Y., and Liu, Y. Au/graphene hydrogel: synthesis, characterization and its use for catalytic reduction of 4-nitrophenol. *Journal of Materials Chemistry*, 22(17):8426-8430, 2012.

[41] Wu, T., Zhang, L., Gao, J., Liu, Y., Gao, C., and Yan, J. Fabrication of graphene oxide decorated with Au–Ag alloy nanoparticles and its superior catalytic performance for the reduction of 4-nitrophenol. *Journal of Materials Chemistry A*, 1(25):7384-90, 2013.

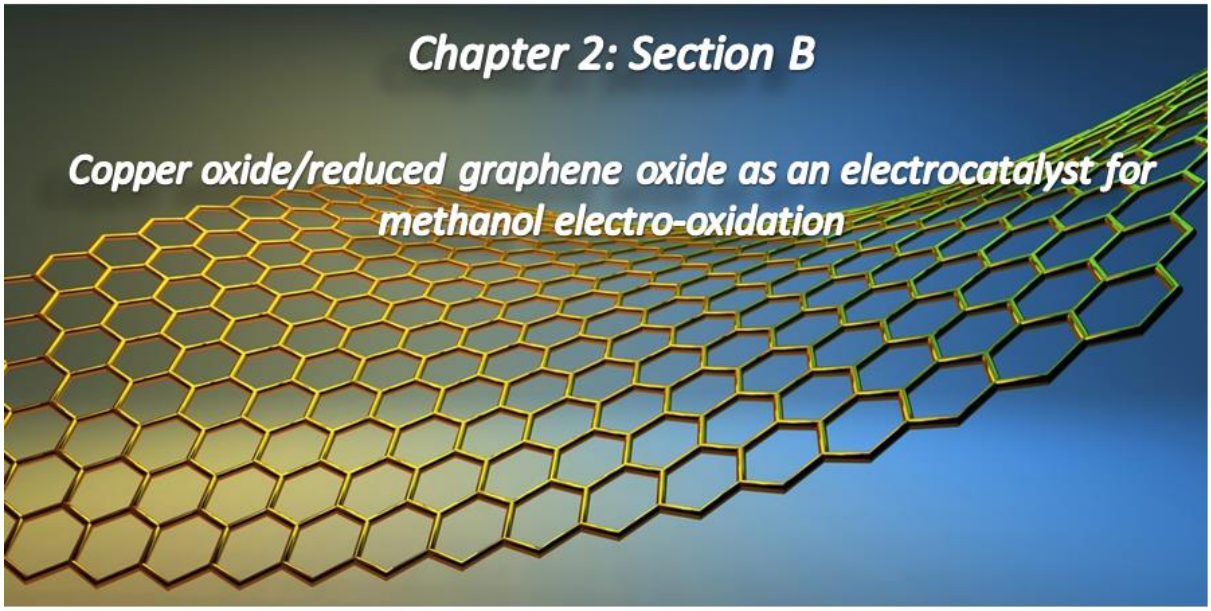

GRAPHICAL ABSTRACT

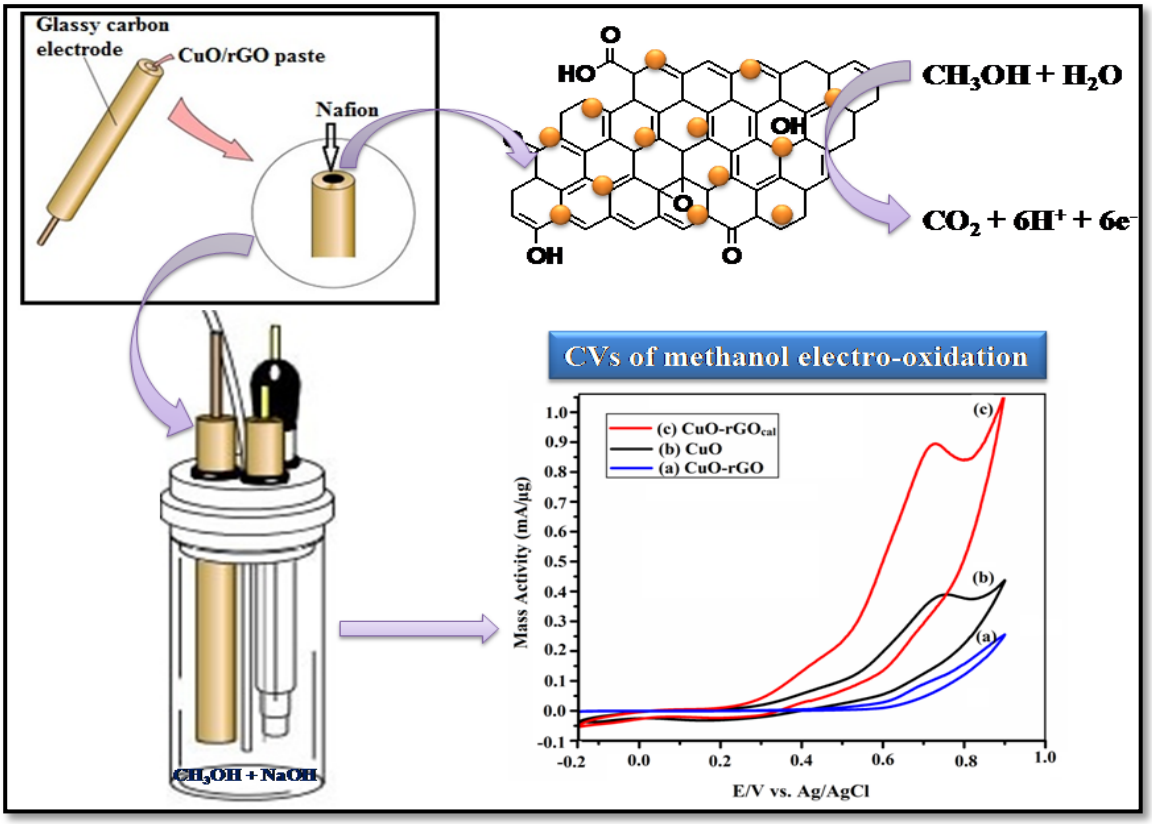

The CuO-rGO nanocomposite, after calcination at 400 °C shows higher electro-catalytic activity towards methanol oxidation in alkaline medium.

2.2 Copper oxide/reduced graphene oxide as an electrocatalyst for methanol electro-oxidation

2.2.1 Introduction

The cornerstone of the world's increasing prosperity and economic growth demands for a clean, affordable and reliable energy source [1]. With the increase energy demand along with the exhaustion of conventional fossil fuels and the rapidly rising environmental problems, the direct methanol fuel cell (DMFC) can be used as an alternate green and sustainable power source [2]. DMFC possesses several significant benefits compared to hydrogen based fuel cells such as high solubility in aqueous electrolyte, high energy density and raw materials can be easily stored and distributed [3]. However, there are two major difficulties preventing DMFCs from successful commercialization which are high manufacturing costs and slow kinetics of the electro-oxidation of methanol at anode [4]. In the last few years, a great number of researches have been carried out to achieve high power density as well as low manufacturing cost of the DMFCs [5]. Till date, Pt catalysts have been recognized to be the efficient single-metal catalyst for DMFCs [6, 7]. Unfortunately, its scarcity, high cost, low power density and poor CO-poisoning tolerance significantly hinder its commercialization and practical use [8]. Metal oxide based catalysts were also used for DMFCs that can provide hydroxyl sources at lower potentials and efficiently undergo a bi-functional mechanism [9-11]. Due to low specific surface area these catalysts suffer from poor electron conductivity. Their catalytic activity can be enhanced by incorporating them on different supporting materials. Carbon nanomaterials have attracted immense and persistent attention as catalytic support because of their extraordinary physical and chemical properties. Reduced graphene oxide (rGO) has a wide variety of applications since its discovery in various fields including fuel cells and other energy storage devices [12-14]. It plays an important role as a support in the fabrication of advanced composite electro-catalysts for high performance DMFCs because of its unique physiochemical properties such as high specific surface area, superior electronic conductivity and excellent stability [15-18].

Metal oxide supported on graphene based nanocomposites have gain tremendous attention because of their low-cost, facile synthesis, high electrocatalytic activity and

durability in DMFC applications [19-21]. Copper oxide (CuO), a well-known p-type semiconductor material has potential in various applications such as gas sensor [22], CO oxidation catalysts [23], solar energy conversion [24], lithium-ion battery anode materials [25], magnetic phase transmitters [26], heterogeneous catalyst [27], optical switches [28], nanofluids [29] and field emitters [30] because of their high catalytic activity as well as their nontoxic nature and affordable cost [31]. Incorporation of CuO nanoparticles onto graphene surface can improve the electrochemical performance of the nanocomposite in comparison with the pure nanoparticles. Mai et. al [32] has synthesized CuO-graphene composite from CuO and graphene oxide (GO) and used as anode material for lithum-ion batteries. The synergetic effect of CuO and GO is beneficial for the improved electrochemical performances of CuO-graphene based composites. As far our knowledge, there is no reported work in literature regarding electrocatalytic application of CuO-rGO towards DMFC. However, several Pt/metal oxide/graphene composites have been reported for DMFCs [Pt/CeO_2/graphene, Pt/MnO_2/graphene, Pt/TiO_2/graphene] where metal oxide acts as a co-catalyst [33-35]. Therefore, the main objective of this work is to synthesize a low cost Pt free electro-catalyst for effective oxidation of methanol.

In this work, CuO-rGO is calcined at 400 °C and used as electrocatalyst towards DMFCs. Interestingly, the calcined nanocomposites showed high electrocatalytic activity towards methanol electro-oxidation in alkaline medium. Having the unique advantage of integrating the facile electron transporting ability of conducting CuO nanoparticles with the supreme electron collecting efficiency of rGO, CuO-$rGO_{calcined}$ provided high durability and low onset potential for methanol oxidation in alkaline medium showing their great potential in DMFCs.

2.2.2 Experimental Section

2.2.2.1 Chemicals

Graphite power, (<20 micron) was purchased from Aldrich. $KMnO_4$, $NaNO_3$, H_2O_2, (30%), CuCl, sodium hydroxide (NaOH), conc. H_2SO_4 HCl and methanol were procured from Merck. Nafion solution was purchased from Sigma-Aldrich.

2.2.2.2 Preparation of GO and CuO-rGO nanocomposites

GO was synthesized from natural graphite power using modified Hummers method [36] followed by exfoliation. CuO-rGO nanocomposite was synthesized by hydrothermal method [37] from mixture of GO and CuCl as mentioned in Chapter 2A with slight modification. Where the product was calcined at 400 °C for 30 min (labeled as $CuO\text{-}rGO_{calcined}$) and used for electrochemical applications. For comparison, CuO nanoparticles were synthesized via direct thermal decomposition method with little modification [38].

2.2.2.3 Characterization

The synthesized samples were characterized by using FTIR, XRD, SEM and EDX analyses. The particle size distribution was studied using Micritrac Flex Software by Dynamic light scattering (DLS) method. The electrochemical analyses were carried out by cyclic voltammetry (CV) using Bio Logic Science Instrument, SP-150 and Power: 110-240 Vac voltammeter.

2.2.2.4 Electrochemical measurements

The electrochemical analyses of the prepared samples were studied using a standard one compartment three electrodes cell where Pt and Ag/AgCl electrodes were used as counter and reference electrodes respectively. The working electrode was a glassy carbon electrode (6 mm diameter) above which the catalyst paste was applied which was prepared by dispersing 12.5 mg of electrocatalyst in 0.5ml of ethanol by ultrasonication for 30 min. Then 0.025mL of 5 wt% Nafion was added onto the paste and air dried for 24h. To measure the methanol electro-oxidation, CV was performed between -0.2 V to 0.9 V at a scan rate of 50 mVs^{-1} in 0.1 M NaOH containing 1 M methanol. To measure the stability of the electrocatalyst the chronoamperometry study was performed for 600 s at a fixed potential of 0.4 V. The durability of the catalyst was further investigated for 100 continuous cycles at scan rate of 50 mVs^{-1}.

2.2.3 Results and discussion

2.2.3.1 FTIR study

Fig. 2.2.1 shows the FTIR spectra of GO, CuO, CuO-rGO and CuO-rGO$_{calcined}$ nanocomposite. The main characteristic peaks of GO (Fig. 2.2.1a) at 1262 cm^{-1}, 1065 cm^{-1} and 1720 cm^{-1} are attributed to the C−O epoxy C−O alkoxy and C=O stretching vibrations, respectively. Peaks at 1621 cm^{-1} and 3416 cm^{-1} correspond to the aromatic C=C stretching vibration and O−H stretching vibration, respectively. The FTIR spectrum of CuO nanoparticles show characteristic infrared absorption peaks in the range of 500-700 cm^{-1} due to Cu−O stretching vibration (Fig. 2.2.1b). In the FTIR spectrum of CuO-rGO nanocompites (Fig. 2.2.1c), the peak intensity of C− O, C=O, and O− H groups decreases significantly and some new peaks appeared in the range of of 500-700 cm^{-1}(at 689 cm^{-1}, 580 cm^{-1} and 505 cm^{-1}) corresponding to Cu−O stretching vibrations confirms formation of CuO-rGO nanocompites. After calcination, the stretching frequencies corresponds to Cu−O stretching vibration is shifted from 689 cm^{-1} to 700 cm^{-1}, 580 cm^{-1} to 573 cm^{-1} and 505 cm^{-1} to 481 cm^{-1} in the FTIR spectrum of CuO-rGO$_{calcined}$ nanocomposite (Fig. 2.2.1d).

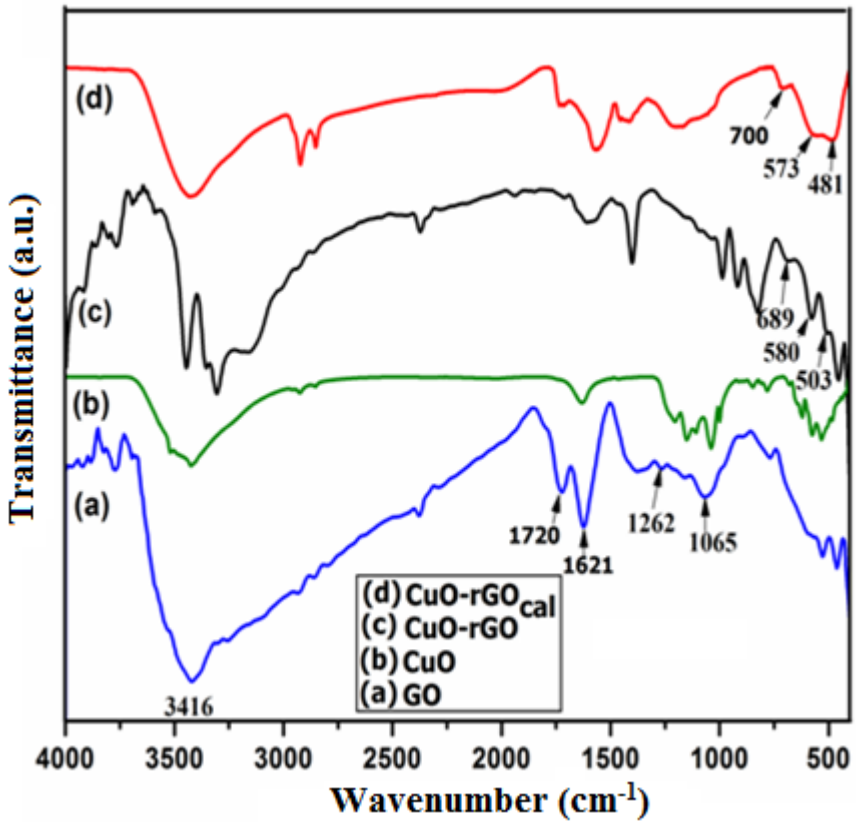

Fig.2.2.1 FTIR spectrum of (a) GO, (b) CuO, (c) CuO-rGO and (d) CuO-rGO$_{calcined}$ nanocomposites

2.2.3.2 XRD analysis

Fig. 2.2.2 shows XRD pattern of GO, CuO, CuO-rGO and CuO-rGO$_{calcined}$ nanocomposite. GO exhibited a strong diffraction peak at 2θ = 11.53^{o} (Fig. 2.2.2a), attributed to the (001) plane due to oxygen containing functional groups on carbon sheets. In the XRD pattern of CuO, CuO, CuO-rGO and CuO-rGO$_{calcined}$ the positions of diffraction peaks matched well with standard CuO and rGO. In the XRD spectrum of CuO, the major peaks located at 2θ = 35.62 ° and 38.9 ° indexed as (111) and (200) planes, respectively, are characteristics for the pure monoclinic end-centered CuO crystal lattice (Fig. 2.2.2b). The XRD spectrum of CuO-rGO exhibits peaks at 2θ values of 32.49° (110), 39.76° (200), 50.32° (112), 53.6° (020), and 61.59° (113) which are consistent with the standard XDR data for the CuO monoclinic phase of the end-centered crystal lattice (Fig. 2.2.2c). Again, the spectrum shows small additional peaks at 25.2° and 44.85° which could be attributed to rGO (Fig. 2.2.2c). After calcinations, in the XRD spectrum of CuO-rGO$_{calcined}$ the peak intensities of the observed peaks hence crystallinity of the composite increases without any peak shifting (Fig. 2.2.2d). Therefore, CuO-rGO$_{calcined}$ becomes notably crystalline after calcinations.

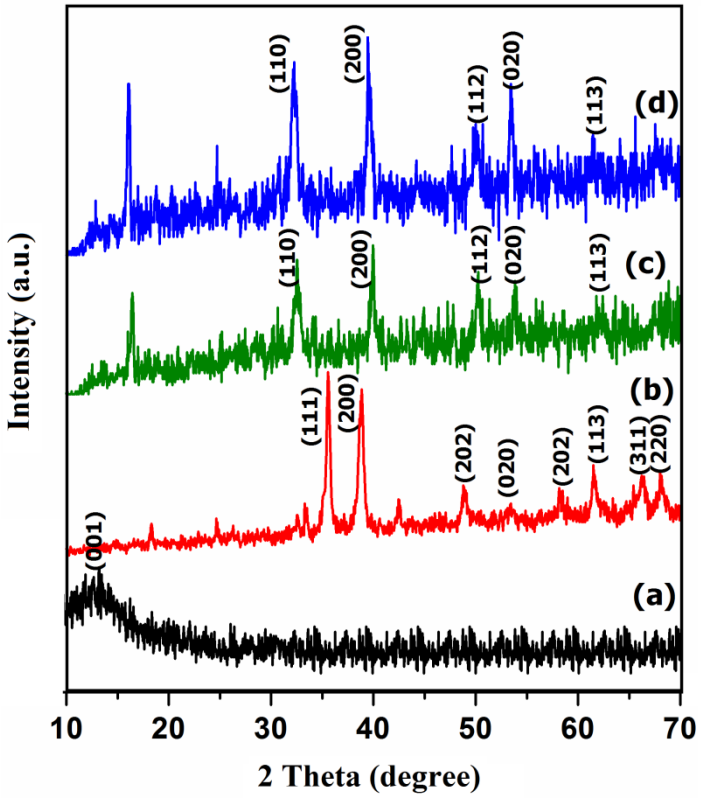

Fig.2.2.2 XRD spectrum of (a) GO, (b) CuO, (c) CuO-rGO and (d) CuO-rGO$_{calcined}$ nanocomposites

2.2.3.3 Raman analysis

Raman spectroscopy is often employed to characterize graphitic materials since it a useful technique for studying disorderness and defects in crystal structure. The intensity ratio between the disorder induced D band and the Raman allowed G band (I_D/I_G) is the measure the measure of disorderness in graphite. The Raman spectra for GO, CuO-rGO and CuO-$rGO_{calcined}$ are shown in Fig.2.2.3 The G bands are seen at 1608 cm^{-1} , 1599 cm^{-1}, and 1594 cm^{-1}, and the D bands are at 1361 cm^{-1}, 1363 cm^{-1}, and 1351 cm^{-1} for GO, CuO-rGO and CuO-$rGO_{calcined}$, respectively. The G band corresponds to an E_{2g} mode of graphite, is related to the vibration of the sp^2-bonded carbon atoms in a two-dimensional hexagonal lattice, while the D band is related to the edges, structural defects that corresponds to the conversion of a sp^2-hybridized carbon to a sp^3-hybridized carbon. The intensity ratio is found to be 0.82 for GO which indicates a high level of disorderness of the GO layers due to the oxidation of graphite. The intensity ratio of CuO-rGO (1.01) and CuO-$rGO_{calcined}$ (1.0) is higher than that for GO, indicating that more defects have been doped into the CuO-rGO. At the same time the change in intensity ratio for the nanocomposite as compared with GO suggests partial reduction of the GO. In addition to the G and D band in the Raman spectrum of

In addition to the G and D band in the Raman spectrum of CuO-rGO and CuO-$rGO_{calcined}$ there were three extra weak peaks at 282, 338 and 599 cm^{-1}, which corresponded to A_g and $2B_g$ CuO phonon peaks [39]. The indicated A_g and $2B_g$ peaks shifted slightly to higher wave numbers and became stronger and sharper after calcination. These results once again demonstrated the existence of both rGO and CuO in the as-prepared nanocomposites.

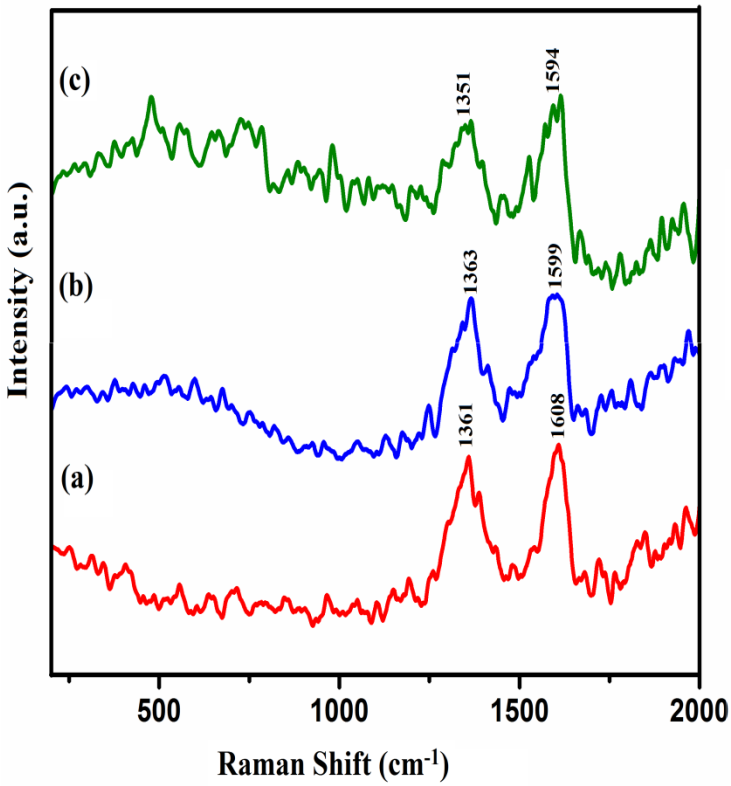

Fig.2.2.3 Raman spectra of (a) GO, (b) CuO-rGO and (c) CuO-rGO$_{calcined}$ nanocomposites

2.2.3.4 SEM and EDX analysis

The morphological changes that occurred on the surface of GO due to incorporation of CuO nanoparticle was examined by scanning electron microscopy. Fig. 2.2.4 shows the SEM images of GO, CuO, CuO-rGO and CuO-rGO$_{calcined}$ nanocomposite. The surface of GO shows a leaf like crumpled structure (Fig. 2.2.4a) while CuO shows spherical structure (Fig. 2.2.4b). A difference in surface morphology between CuO and CuO-rGO nanocomposite is observed. The CuO nanoparticles are uniformly distributed over crumpled, paper-like surface of GO confirming that the incorporation of CuO nanoparticle into GO (Fig. 2.2.4c). It is evident that the surface morphology is improved through calcination. Highly uniform nano-spherical CuO could be observed for the CuO-rGO$_{calcined}$ nanocomposite (Fig. 2.2.4d).

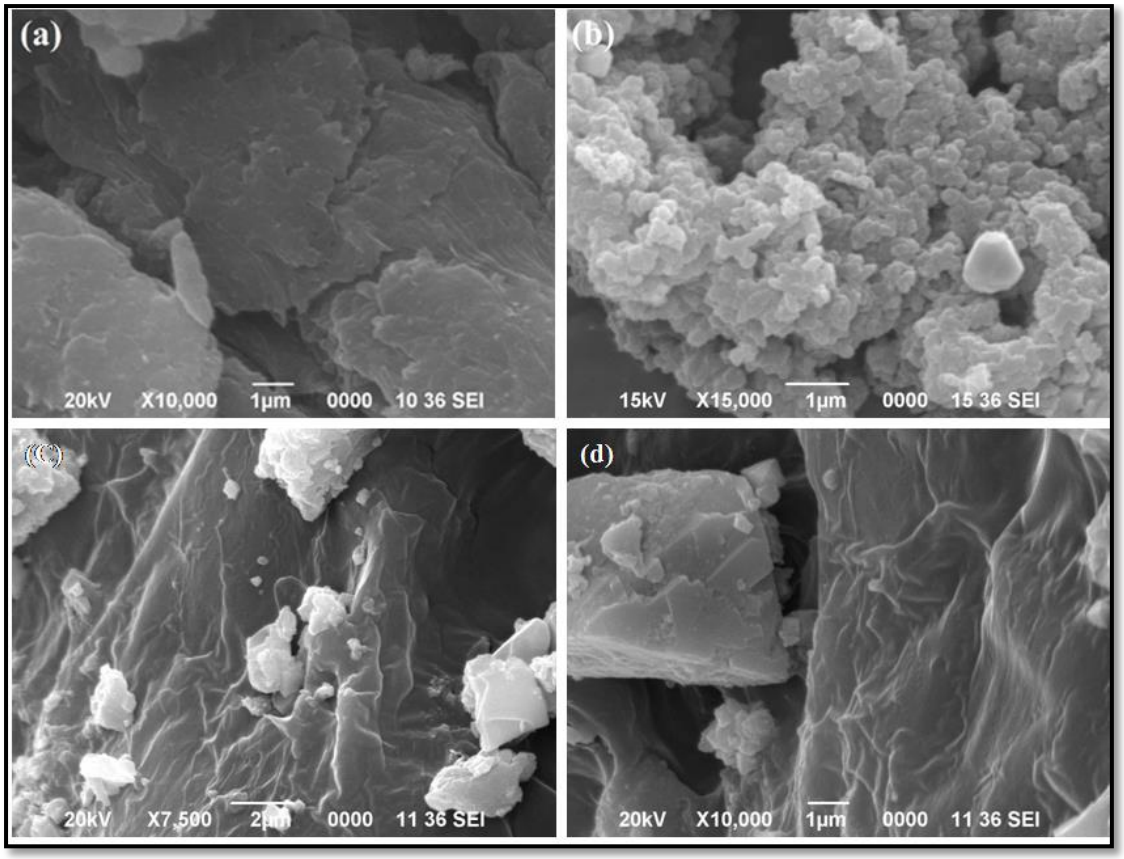

Fig.2.2.4 SEM images of (a) GO, (b) CuO, (c) CuO-rGO and (d) CuO-rGO$_{calcined}$ nanocomposite

In addition, the EDX spectrum of CuO-rGO$_{calcined}$ nanocomposite (Fig. 2.2.5) exhibited the presence of C, O, and Cu elements, further confirming the formation of CuO-rGO composite.

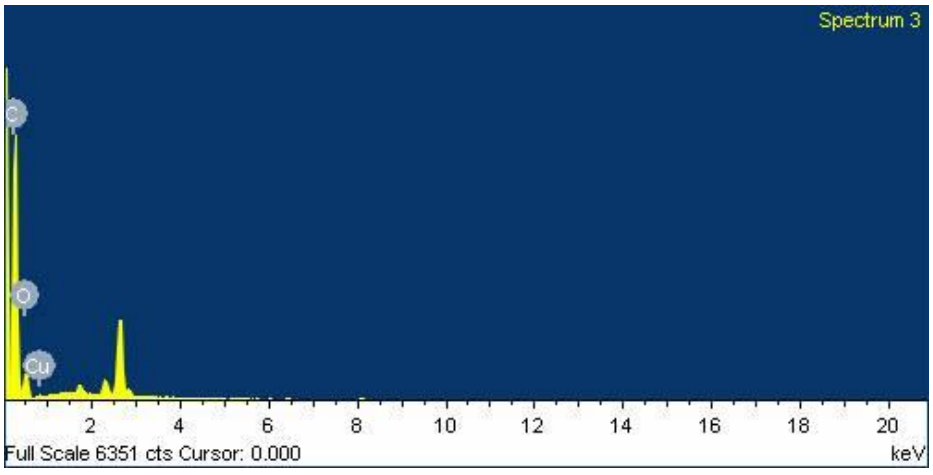

Fig.2.2.5 EDX spectrum of CuO-rGO$_{calcined}$ nanocomposites

2.2.3.5 Particle size distribution

The particle size distribution of CuO-rGO$_{calcined}$ nanocomposite is shown in Fig. 2.2.6. The diameter of the nanocomposite ranged from 0.00096 to 0.00122 micron and the mean diameter is 0.001 micron.

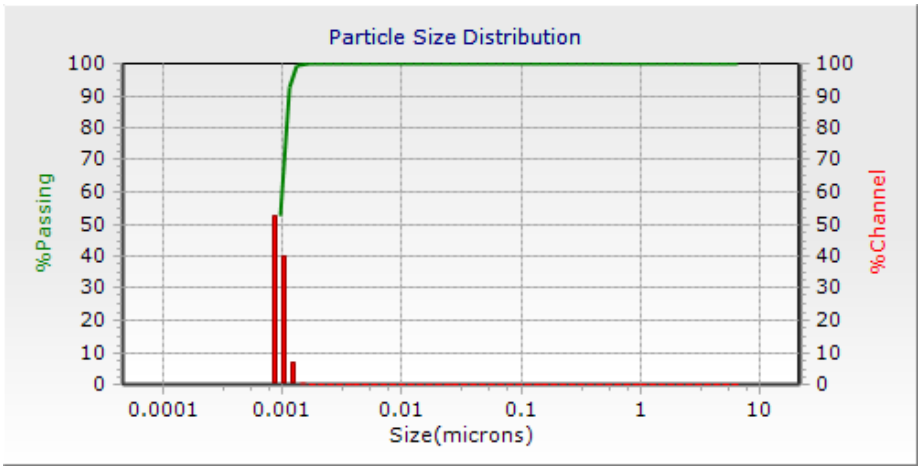

Fig.2.2.6 Particle size distribution of CuO-rGO$_{calcined}$ nanocomposite

2.2.3.6 Electrocatalytic oxidation of methanol

In order to evaluate the electrocatalytic performance of CuO, CuO-rGO and CuO-rGO$_{calcined}$ was studied via CV in alkaline media. Fig. 2.2.7 illustrates the CV of the CuO, CuO-rGO and CuO-rGO$_{calcined}$ recorded in 1.0 M methanol solution containing 0.1 M NaOH. CuO-rGO$_{calcined}$ and CuO show distinct anodic peak towards forward scan, however, there is no characteristic peak for CuO-rGO. This indicates that after calcinations, CuO-rGO nanocomposites shows catalytic activity towards methanol electro-oxidation. The CuO-rGO$_{calcined}$ nanocomposite provided superior electrocatalytic activity for the electro-oxidation of methanol in alkaline medium. During the forward scan, CuO-rGO$_{calcined}$ exhibits a characteristic peak at ca. 0.72 V for the oxidation of methanol, which is lower than that of CuO (0.75 V). A single oxidation peak is generated, revealed the irreversible methanol oxidation. In alkaline medium, the onset potential for the oxidation of methanol at the CuO-rGO$_{calcined}$ is ca. 0.44 V, which is lower than that of the CuO (ca. 0.46 V), Cu NW@rGO-GCE (ca. 0. 48 V), Cu NW-GCE (ca. 0. 6 V) poly-crystalline Cu-GCE (ca. 0.5 V), and Ni–Cu-GCE (ca. 0.5 V) [40]. Moreover, the peak current density for the oxidation of methanol at the CuO-rGO$_{calcined}$ (0.89 mA μg^{-1}) is 2.4 times higher than that of CuO (0.37 mA μg^{-1}), suggesting the superior electrocatalytic activity of the composite. Relative to CuO nanoparticle, the

onset potential and peak potential shifted towards less positive potential at the CuO-$rGO_{calcined}$, revealing the decrease of overpotential for methanol oxidation decreased. In other words, methanol oxidation is occurred more rapidly at CuO-$rGO_{calcined}$ surface. The high catalytic activity can be ascribed to the unique quantum effects between rGO and nanoscale CuO structures [41]; improved conductivity and enhanced surface area of rGO sheets that favoured the improved anchoring of CuO nanoparticles [42]. In addition, the rough surface morphology and the uniform distribution of nano CuO increased the catalytically active sites.

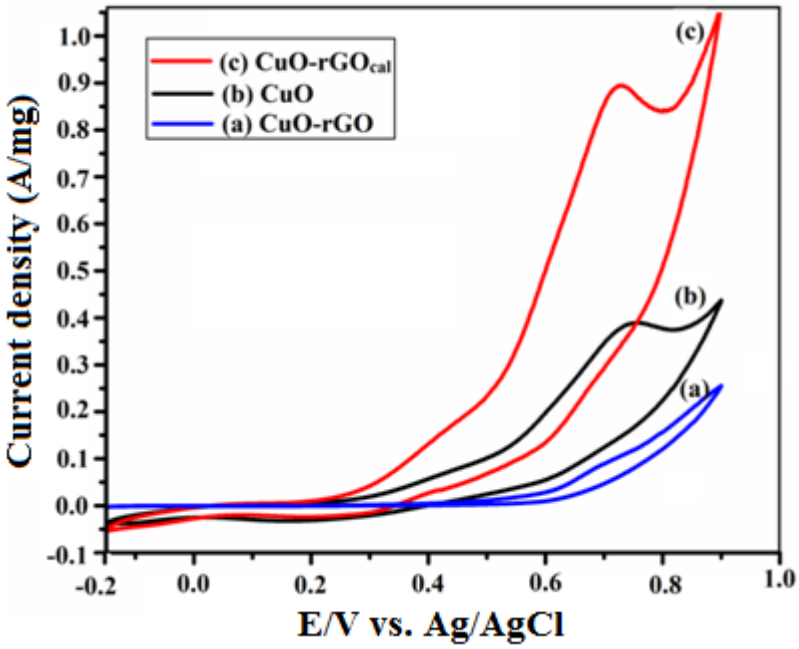

Fig. 2.2.7 CVs of the (a) CuO-rGO, (b) CuO and (c) CuO-$rGO_{calcined}$ in 1.0 M methanol solution containing 0.1 M NaOH. Scan rate: 50 mV s^{-1}.

The mechanism for the electro-oxidation of methanol in alkaline solutions occurred through a mediated electron transfer mechanism. Cu^{III} species that were generated during the anodic sweep, react with intermediates such as CO and OH-like species and complete the oxidation process.

$$Cu^{II} \leftrightarrow Cu^{III} + e^-$$

$$Cu^{III} + (CH_3OH)_{ads} \rightarrow \text{intermediate} + Cu^{II}$$

$$Cu^{III} + \text{intermediate} \rightarrow \text{product} + Cu^{II}$$

The durability of CuO-$rGO_{calcined}$ and CuO was evaluated by chronoamperometry (Fig.2.2.8) for 600s. During the first 200s, a slight decay in the current density was

observed at the CuO-rGO$_{calcined}$, which is attributed to the intermediate products of methanol oxidation that were adsorbed on the surfaces of the catalysts [43]. After that, the current density reached a steady state and remained stable throughout the entire testing period. The current density of the CuO-rGO$_{cal}$ electrode was found to be higher than that of the CuO electrode, revealing the superior durability, good tolerance against the oxidized intermediates and the promising catalytic activity of the composite for the electro-oxidation of methanol. The stability of the CuO-rGO$_{calcined}$ electrode was further investigated for 100 continuous cycles. The voltammetric response decreased slowly with the increasing cycles (Fig. 2.2.9).

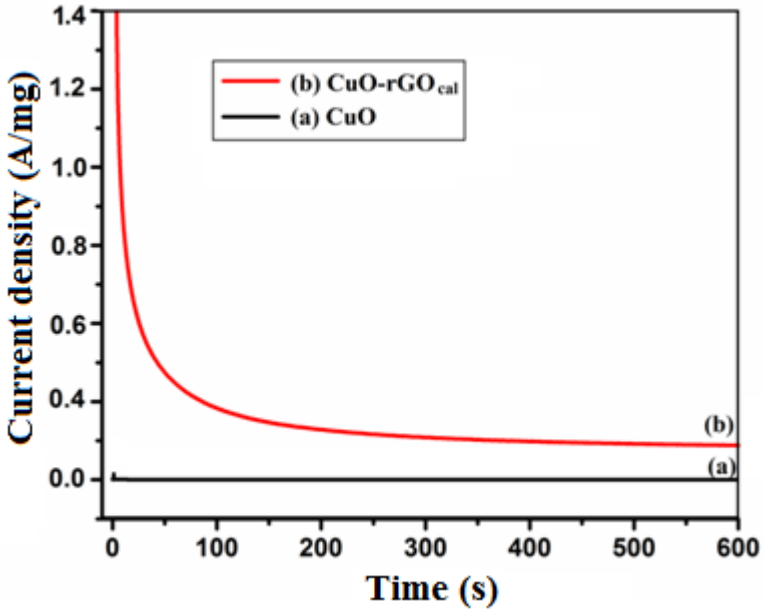

Fig.2.2.8 Chronoamperograms of (a) CuO and (b) CuO-rGO$_{calcined}$ for methanol oxidation in methanol solution (1.0 M) containing 0.1 M NaOH

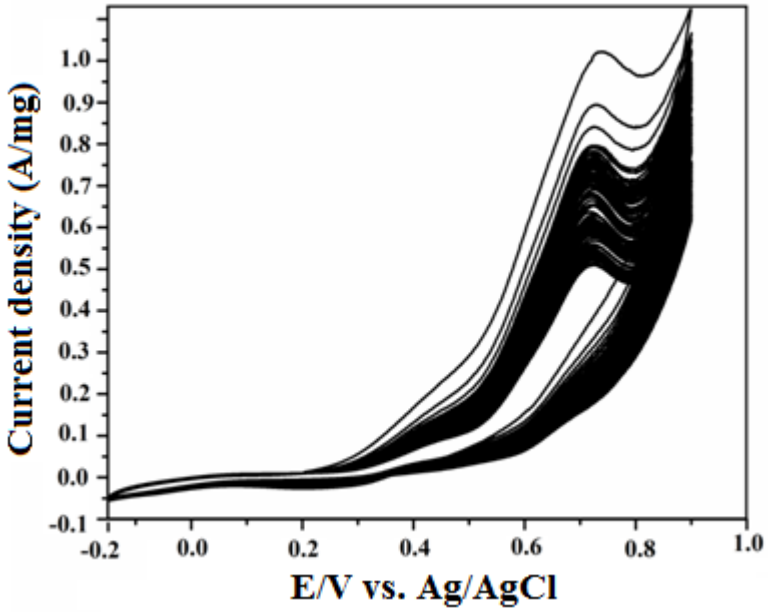

Fig. 2.2.9 CVs of the CuO-rGO$_{cal}$ in 1.0 M methanol solution containing 0.1 M NaOH at scan rate: 50 mV s^{-1} for 100 cycles.

2.2.4 Conclusion

A facile hydrothermal approach was employed for the synthesis of CuO nanoparticles supported on rGO. Under alkaline condition, the electrocatalytic activity of the nanocomposite was higher than that of CuO nanoparticles. The catalyst shows irreversible methanol oxidation at the CuO-rGO$_{calcined}$ surface. The oxidation occurs more rapidly with superior durability, good tolerance against the oxidized intermediates. The proposed facile, synthetic approach opens up new avenues for the fabrication of low-cost catalysts for fuel cell applications.

2.2.5 References

[1] Chu, S. and Majumdar, A. Opportunities and challenges for a sustainable energy future. *Nature*, 488(7411):294-303, 2012.

[2] Li, X. and Faghri, A. Review and advances of direct methanol fuel cells (DMFCs) part I: Design, fabrication, and testing with high concentration methanol solutions. *Journal of Power Sources*, 226:223-240, 2013.

[3] Rodriguez-Reinoso, F The role of carbon materials in heterogeneous catalysis. *Carbon*, 36(3):159-175, 1998.

[4] Chen, C. Y., Chang, J. K., Tsai, W. T., and Hung, C. H. Uniform dispersion of Pd nanoparticles on carbon nanostructures using a supercritical fluid deposition technique and their catalytic performance towards hydrogen spillover. *Journal of Materials Chemistry*, 21(47):19063-19068, 2011.

[5] Steele, B. C. H. and Heinzel, A. Materials for fuel-cell technologies. *In Materials For Sustainable Energy: A Collection of Peer-Reviewed Research and Review Articles from Nature Publishing Group*, 224-231, 2011.

[6] Lin, Y., Cui, X., Yen, C. H., and Wai, C. M. PtRu/carbon nanotube nanocomposite synthesized in supercritical fluid: a novel electrocatalyst for direct methanol fuel cells. *Langmuir*, 21(24):11474-11479, 2005.

[7] Zhao, X., Yin, M., Ma, L., Liang, L., Liu, C., Liao, J., Lu, T., and Xing, W. Recent advances in catalysts for direct methanol fuel cells. *Energy & Environmental Science*, 4(8):2736-2753, 2011.

[8] Zheng, W., Suominen, A., and Tuominen, A. Discussion on the challenges of DMFC catalyst loading process for mass production. *Energy Procedia*, 28:78-87, 2012.

[9] Cao, L., Scheiba, F., Roth, C., Schweiger, F., Cremers, C., Stimming, U., Fuess, H., Chen, L., Zhu, W., and Qiu, X. Novel Nanocomposite Pt/RuO_2xH_2O/Carbon Nanotube Catalysts for Direct Methanol Fuel Cells. *Angewandte Chemie International Edition*, 45(32):5315-5319, 2006.

[10] Song, H., Qiu, X., Guo, D., and Li, F. Role of structural H_2O in TiO_2 nanotubes in enhancing Pt/C direct ethanol fuel cell anode electro-catalysts. *Journal of Power Sources*, 178(1):97-102, 2008.

[11] Chen, Z., Qiu, X., Lu, B., Zhang, S., Zhu, W., and Chen, L. Synthesis of hydrous ruthenium oxide supported platinum catalysts for direct methanol fuel

cells. *Electrochemistry communications*, 7(6):593-596, 2005.

[12] Park, C. H. and Louie, S. G. Tunable excitons in biased bilayer graphene. *Nano letters*, 10(2):426-431, 2010.

[13] Stoller, M. D., Park, S., Zhu, Y., An, J., and Ruoff, R. S. Graphene-based ultracapacitors. *Nano letters*, 8(10):3498-3502, 2008.

[14] Schedin, F., Geim, A. K., Morozov, S. V., Hill, E. W., Blake, P., Katsnelson, M. I., and Novoselov, K. S. Detection of individual gas molecules adsorbed on graphene. *Nature materials*, 6(9):652, 2007.

[15] Huang, H. and Wang, X. Recent progress on carbon-based support materials for electrocatalysts of direct methanol fuel cells. *Journal of Materials Chemistry A*, 2(18):6266-6291, 2014.

[16] Zhou, X., Qiao, J., Yang, L., and Zhang, J. A review of graphene-based nanostructural materials for both catalyst supports and metal-free catalysts in PEM fuel cell oxygen reduction reactions. *Advanced Energy Materials*, 4(8):1301523, 2014.

[17] Mahmood, N., Zhang, C., Yin, H., and Hou, Y. Graphene-based nanocomposites for energy storage and conversion in lithium batteries, supercapacitors and fuel cells. *Journal of Materials Chemistry A*, 2(1):15-32, 2014.

[18] Guo, S. and Dong, S. Graphene nanosheet: synthesis, molecular engineering, thin film, hybrids, and energy and analytical applications. *Chemical Society Reviews*, 40(5):2644-2672, 2011.

[19] Huang, H. and Wang, X. Recent progress on carbon-based support materials for electrocatalysts of direct methanol fuel cells. *Journal of Materials Chemistry A*, 2(18):6266-6291, 2014.

[20] Zhu, C. and Dong, S. Synthesis of graphene-supported noble metal hybrid nanostructures and their applications as advanced electrocatalysts for fuel cells. *Nanoscale*, 5(22):10765-10775, 2013.

[21] Liu, M., Zhang, R., and Chen, W. Graphene-supported nanoelectrocatalysts for fuel cells: synthesis, properties, and applications. *Chemical reviews*, 114(10):5117-5160, 2014.

[22] Zhang, J., Liu, J., Peng, Q., Wang, X., and Li, Y. Nearly monodisperse Cu_2O and CuO nanospheres: preparation and applications for sensitive gas sensors.

Chemistry of materials, 18(4):867-871, 2006.

[23] Luo, M. F., Zhong, Y. J., Yuan, X. X., and Zheng, X. M. TPR and TPD studies of $CuOCeO_2$ catalysts for low temperature CO oxidation. *Applied Catalysis A: General*, 162(1-2):121-131, 1997.

[24] Chang, Y., Teo, J. J., and Zeng, H. C. Formation of colloidal CuO nanocrystallites and their spherical aggregation and reductive transformation to hollow Cu_2O nanospheres. *Langmuir*, 21(3):1074-1079, 2005.

[25] Park, J. C., Kim, J., Kwon, H., and Song, H. Gram-scale synthesis of Cu_2O nanocubes and subsequent oxidation to CuO hollow nanostructures for lithium-ion battery anode materials. *Advanced Materials*, 21(7):803-807, 2009.

[26] Sukhorukov, Y. P., Loshkareva, N. N., Samokhvalov, A. A., Naumov, S. V., Moskvin, A. S., and Ovchinnikov, A. S. Magnetic phase transitions in optical spectrum of magnetic semiconductor CuO. *Journal of magnetism and magnetic materials*, 183(3):356-358, 1998.

[27] Lu, C., Qi, L., Yang, J., Zhang, D., Wu, N., and Ma, J. Simple template-free solution route for the controlled synthesis of Cu $(OH)_2$ and CuO nanostructures. *The Journal of Physical Chemistry B*, 108(46):17825-17831, 2004.

[28] Hansen, B. J., Kouklin, N., Lu, G., Lin, I. K., Chen, J., and Zhang, X. Transport, analyte detection, and opto-electronic response of p-type CuO nanowires. *The Journal of Physical Chemistry C*, 114(6):2440-2447, 2010.

[29] Li, C. C. and Chang, M. H. Colloidal stability of CuO nanoparticles in alkanes via oleate modifications. *Materials Letters*, 58(30):3903-3907, 2004.

[30] Hsieh, C. T., Chen, J. M., Lin, H. H., and Shih, H. C. Field emission from various CuO nanostructures. *Applied Physics Letters*, 83(16):3383-3385, 2003.

[31] Poizot, P. L. S. G., Laruelle, S., Grugeon, S., Dupont, L., and Tarascon, J. M. Nano-sized transition-metal oxides as negative-electrode materials for lithium-ion batteries. *Nature*, 407(6803):496, 2000.

[32] Mai, Y. J., Wang, X. L., Xiang, J. Y., Qiao, Y. Q., Zhang, D., Gu, C. D., and Tu, J. P. CuO/graphene composite as anode materials for lithium-ion batteries. *Electrochimica Acta*, 56(5):2306-2311, 2011.

[33] Cao, J., Chen, Z., Xu, J., Wang, W., and Chen, Z. Mesoporous carbon synthesized from dual colloidal silica/block copolymer template approach as

the support of platinum nanoparticles for direct methanol fuel cells. *Electrochimica Acta*, 88:184-192, 2013.

[34] Girishkumar, G., Hall, T. D., Vinodgopal, K., and Kamat, P. V. Single wall carbon nanotube supports for portable direct methanol fuel cells. *The Journal of Physical Chemistry B*, 110(1):107-114, 2006.

[35] Kakati, N., Maiti, J., Lee, S. H., and Yoon, Y. S. Core shell like behavior of PdMo nanoparticles on multiwall carbon nanotubes and their methanol oxidation activity in alkaline medium. *International Journal of Hydrogen Energy*, 37(24):19055-19064, 2012.

[36] Hummers Jr, W. S. and Offeman, R. E. Preparation of graphitic oxide. *Journal of the American Chemical Society*, 80(6):1339-1339, 1958.

[37] Sarkar, C. and Dolui, S. K. Synthesis of copper oxide/reduced graphene oxide nanocomposite and its enhanced catalytic activity towards reduction of 4-nitrophenol. *RSC Advances*, 5(75):60763-60769, 2015.

[38] Das, D., Nath, B.C., Phukon, P., and Dolui, S. K. Synthesis and evaluation of antioxidant and antibacterial behavior of CuO nanoparticles. *Colloids and Surfaces B: Biointerfaces*, 101:430-433, 2013.

[39] Zhu, J., Zeng, G., Nie, F., Xu, X., Chen, S., Han, Q., and Wang, X. Decorating graphene oxide with CuO nanoparticles in a water–isopropanol system. *Nanoscale*, 2(6):988-994, 2010.

[40] Periasamy, A. P., Liu, J., Lin, H. M., and Chang, H. T. Synthesis of copper nanowire decorated reduced graphene oxide for electro-oxidation of methanol. *Journal of Materials Chemistry A*, 1(19):5973-5981, 2013.

[41] Yan, X. Y., Tong, X. L., Zhang, Y. F., Han, X. D., Wang, Y. Y., Jin, G. Q., Qin, Y., and Guo, X. Y. Cuprous oxide nanoparticles dispersed on reduced graphene oxide as an efficient electrocatalyst for oxygen reduction reaction. *Chemical Communications*, 48(13):1892-1894, 2012.

[42] Tran, P. D., Batabyal, S. K., Pramana, S. S., Barber, J., Wong, L. H., and Loo, S. C. J. A cuprous oxide-reduced graphene oxide (Cu_2O–rGO) composite photocatalyst for hydrogen generation: employing rGO as an electron acceptor to enhance the photocatalytic activity and stability of Cu_2O. *Nanoscale*, 4(13), pp.3875-3878, 2012.

[43] Zhou, C., Liu, Z., Du, X., Mitchell, D. R. G., Mai, Y. W., Yan, Y., and Ringer, S. Hollow nitrogen-containing core/shell fibrous carbon nanomaterials as support to platinum nanocatalysts and their TEM tomography study. *Nanoscale research letters*, 7(1):165, 2012.